HHS Public Access

Author manuscript

Clin Cancer Res. Author manuscript; available in PMC 2023 May 14.

Published in final edited form as:

Clin Cancer Res. 2022 November 14; 28(22): 4907–4916. doi:10.1158/1078-0432.CCR-22-1547.

ImmunoPET Imaging with ^{89}Zr-labeled Atezolizumab Enables *In Vivo* Evaluation of PD-L1 in Tumorgraft Models of Renal Cell Carcinoma

Aditi Mulgaonkar[1], **Roy Elias**[2,3], **Layton Woolford**[2,3], **Bing Guan**[1], **Kien Nham**[1], **Payal Kapur**[2,4,6], **Alana Christie**[2,5], **Vanina T. Tcheuyap**[2,3], **Nirmish Singla**[2,4], **I. Alex Bowman**[2,3], **Christina Stevens**[2,3], **Guiyang Hao**[1], **James Brugarolas**[2,3], **Xiankai Sun**[1,7]

[1]Department of Radiology, University of Texas Southwestern Medical Center, Dallas, TX, USA

[2]Kidney Cancer Program, Simmons Comprehensive Cancer Center, University of Texas Southwestern Medical Center, Dallas, TX, USA

[3]Department of Internal Medicine, Hematology-Oncology, University of Texas Southwestern Medical Center, Dallas, TX, USA

[4]Department of Urology, University of Texas Southwestern Medical Center, Dallas, TX, USA

[5]Department of Population and Data Sciences, University of Texas Southwestern Medical Center, Dallas, TX, USA

[6]Department of Pathology, University of Texas Southwestern Medical Center, Dallas, TX, USA

[7]Advanced Imaging Research Center, University of Texas Southwestern Medical Center, Dallas, TX, USA

Abstract

Purpose: Immune checkpoint inhibitors (ICIs) targeting the programmed cell death protein 1 and its ligand (PD-1/PD-L1) have transformed the treatment paradigm for metastatic renal cell carcinoma (RCC). However, response rates to ICIs as single agents or in combination vary widely and predictive biomarkers are lacking. Possibly related to the heterogeneity and dynamic nature of PD-L1 expression, tissue-based methods have shown limited value. Immuno-positron emission tomography (immunoPET) may enable noninvasive, comprehensive, and real-time PD-

Correspondence to: James Brugarolas, M.D., Ph.D., University of Texas Southwestern Medical Center, Department of Internal Medicine, ND3.504, 5323 Harry Hines Blvd, Dallas, Texas 75390-8852, James.Brugarolas@UTSouthwestern.edu, Phone: +1-214-648-4059; Xiankai Sun, Ph.D., University of Texas Southwestern Medical Center, Department of Radiology, NE3.240, 5323 Harry Hines Blvd, Dallas, Texas 75390-8542, Xiankai.Sun@UTSouthwestern.edu, Phone: +1-214-645-5978.

Authors' contributions

X.S. and J.B. conceived the study, proposed, and supervised the design and implementation of the project. A.M. was involved in project design and coordination, radiotracer development, manuscript writing, and post-quantification data interpretation; R.E. performed clinical data collation, analysis, and participated in data interpretation and manuscript writing; L.W. was involved in TG line development, patient TG line selection, tissue collection for IHC post-imaging, and coordination with the imaging, clinical and pathology teams; K.N. performed the PET imaging procedures and PET quantification (blinded analysis); B.G. performed the radiolabeling procedures and western blot analysis to confirm PD-L1 expression in the cell lines used in the study; P.K. performed the IHC procedures and data interpretation (blinded analysis); A.C. performed statistical analysis of the data; N.S. performed clinical data collation; I.A.B. assisted with clinical aspects; V.T.T. and C.S. were involved in TG line development and performed tissue collection for IHC post-imaging; G.H. was involved in project design, and performed the chelator number determination by LC-MS analysis.

Authors' Disclosures

No conflicts of interest were reported by the authors.

L1 detection. Herein, we systematically examined the performance of immunoPET for PD-L1 detection relative to immunohistochemistry (IHC) in an RCC patient-derived tumorgraft (TG) platform.

Experimental Design: Eight independent RCC TGs with a wide range of PD-L1 expression (0 – 85%) were evaluated by immunoPET. Uptake of ^{89}Zr-labeled atezolizumab ([^{89}Zr]Zr-DFO-ATZ) was compared to PD-L1 expression in tumors by IHC through double-blind analyses. Clinical outcomes of ICI-treated patients whose TGs were examined were analyzed to evaluate the clinical role of immunoPET in RCC.

Results: ImmunoPET with [^{89}Zr]Zr-DFO-ATZ (day 6/7 post-injection) revealed a statistically significant association with PD-L1 IHC assays ($p = 0.0014$; correlation $\rho_{XY} = 0.78$). Furthermore, immunoPET can be used to assess the heterogeneous distribution of PD-L1 expression. Finally, studies in the corresponding patients ($n = 4$) suggest that PD-L1 signal may influence ICI responsiveness.

Conclusions: ImmunoPET with [^{89}Zr]Zr-DFO-ATZ may enable a thorough and dynamic assessment of PD-L1 across sites of disease. The power of immunoPET to predict ICI response in RCC is being explored in an ongoing clinical trial (NCT04006522).

Keywords

ImmunoPET; Atezolizumab; Kidney cancer; Renal cancer; PD-L1; PD-1; Immunotherapy; Immune checkpoint inhibitors; Predictive biomarkers

Introduction

Renal cell carcinoma (RCC) accounts for ~ 4% of all cancer cases in the United States, with estimated 79,000 new cases and 13,920 deaths in 2022 (1). The treatment landscape for RCC has changed dramatically over the past 5 years with the introduction of immune checkpoint inhibitor (ICI) therapy (2–7). Among immune checkpoint proteins leveraged for immunotherapy, the programmed cell death 1 receptor (PD-1) and its ligand (PD-L1) play a central role (8,9). PD-1/PD-L1 dampen the host immune system to protect against autoimmunity (8,10). While PD-1 expression is restricted to activated hematopoietic cells including lymphocytes and antigen presenting cells, PD-L1 is found in both hematopoietic and non-hematopoietic tissues (11). In many malignancies, the PD-1/PD-L1 pathway is hijacked by cancer cells to suppress an anti-tumor immune response (12). To date, the United States Food and Drug Administration (FDA) has approved six monoclonal antibodies (mAbs) targeting PD-1 or PD-L1 across 19 cancer types and two tissue-agnostic conditions (13).

Clinical responses to ICI therapies are heterogeneous. While long lasting responses occur in a subset of RCC patients, the disease ultimately progresses in over 50% (2,7,9,14–16). Predictive biomarkers are lacking and this represents an unmet medical need. Tissue-based PD-L1 analyses have failed to show consistent results. In CheckMate 025, a trial leading to FDA approval of nivolumab for patients with previously treated metastatic RCC, a correlation between overall survival and PD-L1 expression was not observed (7). The CheckMate 214 study, which compared the combination of an anti-PD-1 mAb (nivolumab)

with an anti-CTLA4 mAb (ipilimumab) to standard-of-care sunitinib in treatment of naïve metastatic RCC patients, showed improved survival in patients with baseline PD-L1 tumor expression (≥ 1% PD-L1), but this failed to reach statistical significance (2). These controversial results likely reflect confounding factors. Tissue-based PD-L1 analyses are limited by the samples utilized. Biopsies provide minimal amounts of tissue from a single site, and given PD-L1 heterogeneity, the results may not be representative. An alternative is afforded by surgical resection specimens, which enable broader studies, but the specimens are often dated and may not be representative of the remaining sites of disease in the patient. In addition, immunohistochemistry (IHC) assays are limited by the particular anti-PD-L1 antibody utilized, and substantial heterogeneity has been observed (17,18). Finally, there are limitations with scoring pertaining to the type of cell, signal intensity and localization, as well as the percentage of positive cells set as a threshold for positivity or negativity.

Recent technological advances in immuno-positron emission tomography (immunoPET) have made it possible to noninvasively and quantitatively assess immune system pathways in real-time. Indeed, immunoPET imaging of PD-L1 with a ^{89}Zr-labeled deferoxamine conjugate of atezolizumab, a fully humanized therapeutic anti-PD-L1 mAb with a mutant Fc fragment ([^{89}Zr]Zr-DFO-ATZ), has been evaluated in a clinical trial in patients with bladder, breast, and non-small cell lung cancer (19). Despite the small sample size (n = 22), tumoral PET outperformed IHC as a predictive marker of response to ATZ in this first-in-human study of immunoPET imaging of PD-L1.

We explored immunoPET with [^{89}Zr]Zr-DFO-ATZ in RCC and previously reported a case study showing increased uptake of [^{89}Zr]Zr-DFO-ATZ in a patient-derived tumorgraft (TG) mouse model corresponding to a patient with metastatic RCC, who experienced a remarkable and lasting response to nivolumab (20). In this work, we present systematic analyses of RCC TG lines (n = 8) expressing a wide range of PD-L1 (0 – 85%), including the case study. Through a double-blind analysis, we evaluated the correlation of tumoral PET signal with corresponding PD-L1 by IHC to validate the use of immunoPET for noninvasive PD-L1 assessment.

Materials and Methods

Production and characterization of DFO-ATZ and [^{89}Zr]Zr-DFO-ATZ

The preparation of DFO-ATZ was carried out by our previously reported procedure with minor modifications (20). Specifically, we introduced a liquid chromatography–mass spectrometry (LC-MS) method to quantify the molar ratio of DFO (Macrocyclics, # B-705) *vs.* ATZ (Genentech/Roche) in the conjugate. For each batch of DFO-ATZ production, our quality control (QC) procedures included assessment of chemical purity by high performance liquid chromatography (HPLC), radiolabeling efficiency with ^{89}Zr radionuclide, and binding specificity to the target PD-L1 protein by cell assays.

The ^{89}Zr labeling of DFO-ATZ was performed in the Cyclotron and Radiochemistry Program at University of Texas Southwestern Medical Center (UT Southwestern) using a GE PETtrace 880 cyclotron (GE Healthcare) for in-house ^{89}Zr production following current good manufacturing practices (CGMP) for radiotracer production for clinical use.

Determination of the molar ratio of DFO per ATZ antibody molecule in DFO-ATZ conjugates

The averaged molar ratio of DFO/ATZ in the prepared DFO-ATZ was determined by LC-MS. The sample was loaded to an Agilent 6540 Q-TOF LC-MS system equipped with an Agilent 300 SB-C3 RRHD 1.8 μm LC column, 2.1 × 100 mm. The HPLC gradient was set to: 90% to 80% A [0.1% formic acid (Sigma-Aldrich, #399388) in water] from 0 – 4 min, 80% to 10% A from 4 – 5 min, and then 90% to 100% B [0.1% formic acid in acetonitrile (Sigma-Aldrich, #AX0156)] from 5 – 10 min. Dual Agilent Jet Stream Electrospray Ionization (AJS ESI) was used as the time-of-flight (TOF) MS ion source, and the sample was run at the positive polarity mode. Profile MS data was acquired for protein deconvolution data analysis using the Agilent MassHunter Qualitative Analysis with BioConfirmProteinDigest version B06.00. From the deconvolution results, peaks corresponding to unmodified ATZ and DFO-ATZ were manually integrated. The area of each peak was obtained for the calculation of DFO number per ATZ: $N = R_0 \times 0 + R_1 \times 1 + R_2 \times 2 + \cdots + R_n \times n$. (N is the chelator number per ATZ; R_0, R_1, R_2 or R_n is the percentage of the peak area corresponding to DFO-ATZ with 0, 1, 2, or n of DFO chelator), respectively.

Binding affinity

Binding affinity experiments utilized the PD-L1 expressing A20 lymphoma cell line (ATCC, # TIB-208, RRID: CVCL_1940), which was maintained at 37 °C in 5% CO_2 in RPMI-1640 medium (Sigma-Aldrich, #R8758), supplemented with 10% fetal bovine serum (Sigma-Aldrich, #F2442) and 1% penicillin-streptomycin antibiotics (Sigma-Aldrich, #P0781). Cells were incubated with the DFO-ATZ conjugate at different dilutions (from 10 μg/mL to 5 pg/mL, 5-fold dilutions) for 20 min at room temperature. After incubation, the cells were washed twice with 1× phosphate buffered saline (PBS) (Sigma-Aldrich, #D8537), and stained by PE-anti-human IgG secondary antibody (Biolegend, #366903, RRID: AB_2876689). Cells were then washed again with PBS and analyzed using a CytoFLEX (Beckman Coulter) flow cytometer. The binding affinity was determined by estimating the EC_{50} values from mean fluorescent intensity (MFI) using GraphPad Prism 8.0.

Animal models

Eight RCC patient-derived TG lines with varying levels of PD-L1 expression were expanded using NOD/SCID (NOD.CB17-Prkdc^{scid}) mice by surgical implantation of the tumors in the shoulder flank or thigh regions (21). They were as follows: XP783 (cohort [c] 17: 60 – 85% PD-L1, n = 3), XP945 (c1: 40 – 60%, n = 3; c6: 55 – 70% PD-L1, n = 3), XP925 (c1: 10 – 15% PD-L1, n = 3), XP813 (c8: 1 – 5% PD-L1, n = 3), XP955 (c1: 60 – 70% PD-L1, n = 3), XP818 (c24: 0% PD-L1, n = 4), XP258 (c29: 1 – 10% PD-L1, n = 2), and XP490 (c25: 40 – 75% PD-L1, n = 3). The percentage of PD-L1 expression reported was obtained through *ex vivo* IHC analysis of the explanted TG tumors after immunoPET. Throughout the experiment, animals were housed in laminar flow cages maintained at ~22 °C with ~55% relative humidity in a 12-hour light/dark cycle. Mice were permitted free access to autoclaved water and commercial food, throughout the experiment. When tumor sizes reached ≥ 50 mm^3, immunoPET scans were performed on the tumor-bearing mice,

from whom the tumors would be later excised for IHC analysis at the end of imaging. Imaging reconstruction and quantitative analyses were conducted by the immunoPET team, while histology studies were completed by the histopathology core of the Kidney Cancer Program. Experiments were based on an Institutional Animal Care and Use Committee protocol in compliance with the United States Public Health Service Standards and National Institutes of Health guidelines.

Mouse PET/CT imaging studies

ImmunoPET scans were performed on a Siemens Inveon PET/CT Multi-modality System (Knoxville, TN) with an effective spatial resolution of 1.4 mm at the center of field of view (FOV). Each mouse received ~3.7 MBq of [^{89}Zr]Zr-DFO-ATZ (equivalent to ~29 – 52 μg of DFO-ATZ) intravenously via the tail vein (Day 0). Static PET scans were performed from day 1 up to day 7 post injection (p.i.) for 15 to 45 min on mice anesthetized with isoflurane. CT scanning was performed to obtain the required anatomical information for data analysis. CT projections (360 steps/rotation) were acquired with a power of 80 kVp, current of 500 μA, exposure time of 142 ms, binning of 4, and effective pixel size of 102 μm. The acquired static PET data were reconstructed using the 3D Ordered Subsets Expectation Maximization (OSEM3D/MAP) algorithm. The CT reconstruction protocol with a downsample factor of 2 was set to interpolate bilinearly and used a Shepp-Logan filter. The obtained PET and CT images were co-registered using the manufacturer's software package for image and data analysis. As part of the double-blinded study, PET data quantification was blinded to the grouping information of the TG bearing mice. Guided by CT, the regions of interest (ROIs) were drawn manually, encompassing the coronal, axial, and sagittal planes of the tissue. The uptake of [^{89}Zr]Zr-DFO-ATZ in each ROI was calculated as percentage injected dose per gram (% ID/g).

Histogram analysis of PET signal in ROIs

A voxel-based analysis of PET ROI data (22) was performed to evaluate the intratumoral uptake distribution of [^{89}Zr]Zr-DFO-ATZ using two representative TG lines (XP945, n = 6 and XP818, n = 4). The resultant voxel-based data were exported in excel, in which histograms of data were generated (0.5% ID/g bin width, starting from 0.25% ID/g) using GraphPad Prism 8.0. Since the absolute frequency of voxels falling into a bin partly depends on the number of voxels analyzed, the probability distribution was then calculated by normalizing the histograms to the total number of voxels analyzed, which varied with tumor size. A mixed model statistical analysis was performed to compare the radiotracer uptake curves using a compound symmetric covariance structure for PET voxels measured within the same mouse, where the uptake in the muscle was used as the background signal (non-specific uptake) in each mouse.

Histology/Immunohistochemistry

After PET/CT scans, the animals were sacrificed. Tumorgrafts were collected immediately, fixed in 10% neutral-buffered formalin for 48 hours, and then stored in 70% ethanol at −20 °C. The samples were processed and embedded in paraffin blocks for histology and PD-L1 IHC after the radioactivity decayed (~33 days). Prior to fixation, the tumors were measured for volume estimations (length, width, and height). PD-L1 (1:300, BioCare, #ACI

3171A) IHC was performed using a Dako Autostainer Link 48 after its standardization and validation using 10 ccRCC tumors with a wide range of PD-L1 expression as controls (Dako, #22C3 antibody) from our Clinical Laboratory Improvement Amendments (CLIA) certified laboratory. Positive and negative controls with known PD-L1 expression were used with each run of immunostaining. Combined Positive Scores (CPS) were recorded as the number of PD-L1 staining cells (both tumor and other stromal cells) divided by the total number of tumor cells evaluated, multiplied by 100 (23). The analysis was performed by a trained pathologist (P.K.) blinded to other results using recommended guidelines (https://pathology-education.agilent.com/en-us/home.html).

Clinical data analysis

Under the purview of an Institutional Review Board (IRB)-approved protocol (STU 012011–190), clinical and pathologic information of the 8 patients contributing tissues for TG generation was retrospectively compiled. Histological data were confirmed by a genitourinary pathologist (P.K.). For patients who received immunotherapy (n = 4), International Metastatic RCC Database Consortium (IMDC) risk scores were calculated at the time of immunotherapy initiation. Best objective response to ICI was measured using principals from the Response Evaluation Criteria in Solid Tumors (RECIST) version 1.1. Tumor burden was reported as the sum of the longest diameters of target lesions. For clinical data analyses, baseline clinicopathologic characteristics were tabulated and evaluated using descriptive statistics.

Statistical analysis

GraphPad Prism 8.0 was used for data analyses, except where mixed models were used, which were conducted in SAS 9.4 (SAS). All data analyses were completed at an alpha value = 0.05 and two-tailed p-values without correction for multiple comparisons. Mixed-effects correlation analyses were performed using the method described by Lam et al. (24), which removes the variation due to individual TG. A mixed model statistical analysis was performed to evaluate the association of tumor uptake values and tumor-to-muscle uptake ratios, individually, with the corresponding PD-L1 IHC measurements, using the pooled data (n = 25) from all 8 RCC TG lines. These analyses were performed with a compound symmetric covariance structure for mice within the same TG model. The distribution of tumor uptake voxels [mean 4.62% ID/g for XP945 *vs.* 3.5% ID/g for XP818] in two representative TG lines were also compared using a mixed model analysis, with a compound symmetric covariance structure for voxels from the same mouse, where the uptake in the muscle was used as the background signal (non-specific uptake) in each mouse. In addition, we centered the voxel distributions by XP line on the same median and used the Kolmogorov-Smirnov two sample test to determine if there was a difference in the shapes of the two distributions.

Data Availability Statement

The data used and analyzed in this manuscript are available from the corresponding authors (J.B. & X.S.) upon request.

Results

[^{89}Zr]Zr-DFO-ATZ retains PD-L1 binding affinity and specificity

We conjugated DFO to ATZ. As shown in Fig. 1A, the DFO-ATZ conjugation resulted in four species varying the DFO chelator number per ATZ molecule from 0 to 3. The apparent number of DFO per ATZ was calculated to be 0.98 according to the molecular distribution determined by LC-MS analysis. An *in vitro* cell assay using the PD-L1 expressing A20 lymphoma cell line (Fig. 1B) showed that the PD-L1 binding affinity of DFO-ATZ was not significantly undermined relative to the unconjugated antibody (DFO-ATZ: EC_{50} = 21.14 ± 11.9 pM *vs.* intact ATZ: EC_{50} = 34.9 ± 13.5 pM). The immunoreactivity of [^{89}Zr]Zr-DFO-ATZ was determined by a Lindmo assay to be 86 ± 4% (Fig. 1C). Furthermore, the PD-L1 binding specificity of [^{89}Zr]Zr-DFO-ATZ was confirmed by a cell-based blocking assay, in which co-incubation with ~100 times excess of ATZ (~ 6 ng) completely blocked the binding of [^{89}Zr]Zr-DFO-ATZ (Fig. 1D).

Tumorgraft resource affords state-of-the-art platform for [^{89}Zr]Zr-DFO-ATZ evaluation

To further evaluate [^{89}Zr]Zr-DFO-ATZ, we leveraged our TG resource involving >100 TG models generated from surgical specimens of RCC patients implanted orthotopically in immunocompromised mice without additives or disaggregation (21). We selected TG lines with PD-L1 expression ranging from 0% to 85% (n = 8). TGs were derived from a clinically heterogeneous group of patients (Table 1). Two (25%) cases were derived from women, and 3 (37.5%) from ethnic minorities. Four (50%) TGs were generated from metastatic sites (bone, spinal cord [n = 2], and retroperitoneum) and the remainder from primary tumors. Histologically, 7 (87.5%) were clear cell RCC (ccRCC) and one was a papillary RCC (pRCC). Generally, TG PD-L1 expression by IHC was similar to that of the corresponding patient tumor.

ImmunoPET signal correlates with PD-L1 tissue levels in TG models

Determining an optimal time point and reference tissue for quantitative immunoPET imaging analysis: TG bearing mice were injected with ~ 3.7 MBq (equivalent to ~ 29 – 52 μg of DFO-ATZ) [^{89}Zr]Zr-DFO-ATZ (n ≥ 3 per line, except XP258 with n = 2). This dose was selected based on a previously reported dose-escalation study, where a dose-dependent biodistribution was observed upon co-injection of 30 – 90 μg of unlabeled ATZ with ~8 μg ^{111}In-labeled ATZ (25). ImmunoPET/CT imaging was performed from day 1 up to day 7. PET data were reconstructed using an OSEM3D/MAP algorithm and the PET and CT images were co-registered. Guided by the CT, ROIs were drawn encompassing coronal, axial, and sagittal planes. The uptake of [^{89}Zr]Zr-DFO-ATZ in each ROI was calculated as % ID/g. Different organs were evaluated and kinetic analyses were performed. Highest levels of [^{89}Zr]Zr-DFO-ATZ were observed in the tumors as well as heart, liver, kidneys, and spleen (Supplementary Fig. S1 - S2). PET signal demonstrated a gradual and steady decline in the heart, liver, kidneys, and tumors over several days, likely reflective of clearance of the antibody from the circulation over time. In contrast, bone uptake increased by 1.5 – 2 fold over the study period, which can be attributed to the accumulation of ^{89}Zr after lysosomal degradation of [^{89}Zr]Zr-DFO-ATZ, and is consistent with other reports (26,27). As a reservoir of PD-L1 expressing immune cells, the spleen

showed high and fairly consistent uptake throughout the imaging window. Muscle uptake was low (~ 1.5% ID/g) and remained steady throughout the imaging period (Supplementary Fig. S1). Thus, we chose to focus our analyses on tumor-to-muscle (T/M) uptake ratios (Supplementary Table S1). Given maximal systemic clearance of [^{89}Zr]Zr-DFO-ATZ at day 6 ± 1 p.i. (Fig. 2 and Supplementary Fig. S2), this time point was used for correlation analyses.

Like patient RCCs, TGs grow at variable rates within their mouse hosts (21,28), and we asked whether the PET signal may be affected by tumor size. As shown in Supplementary Fig. S3, [^{89}Zr]Zr-DFO-ATZ tumor uptake was fairly consistent across a broad range of tumor sizes (53 mm^3 – 3,960 mm^3) for the different TG lines.

Mixed model statistical analysis of immunoPET: Representative immunoPET images from seven TG lines on day 6 p.i. of [^{89}Zr]Zr-DFO-ATZ are shown in Fig. 2 (an image of XP258 is not shown as only one mouse survived to the end of the experiment). Following image acquisition, tumors were harvested for histological and IHC analyses (Fig. 2). Tumor samples from the corresponding patient tumors were incorporated as a reference. To evaluate the performance of [^{89}Zr]Zr-DFO-ATZ immunoPET imaging, we conducted a repeated measures linear regression analysis. We compared immunoPET tumor uptake values and T/M signal ratios (Supplementary Table S1) to the corresponding IHC-derived tumor PD-L1 expression levels (n = 25 samples representing 8 TG lines). The regression model accounted for the IHC variation among individual mice within a TG line. These studies showed a statistically significant association between IHC PD-L1 level and [^{89}Zr]Zr-DFO-ATZ immunoPET using either T/M ($p = 0.0014$) or tumor uptake ($p = 0.030$). The correlation (ρ_{XY}) was 0.78 for T/M with a slope of 0.029 ± 0.008 (95% confidence interval (CI) = 0.013 – 0.045) (Fig. 3A), and 0.57 for tumor uptake with a slope of 0.014 ± 0.006 (95% CI = 0.001 – 0.027) (Supplementary Fig. S4).

Voxel-based uptake distribution analysis of heterogeneous PD-L1 expression: We observed intratumoral variation in both immunoPET signal and PD-L1 expression by IHC (Fig. 2). In order to further assess the capability of immunoPET to detect heterogeneous intratumoral PD-L1 expression, we carried out a voxel-to-voxel analysis of tumor uptake in XP945 (PD-L1 IHC 40 – 70%) using the corresponding data in XP818 (PD-L1 IHC 0%) as control. A mixed model analysis was performed to compare the uptake distribution difference of [^{89}Zr]Zr-DFO-ATZ in these two TG lines, in which the uptake in the muscle was used as non-specific signal in each mouse to level out the background differences among mice. The analyis revealed not only a statistically significant difference ($p = 0.0024$) in the intratumoral voxel distributions of [^{89}Zr]Zr-DFO-ATZ, but also a difference in the shapes of the distributions centering on the same median (Kolmogorov-Smirnov $p < 0.0001$) (Fig. 3B). While the radiotracer's distribution in XP818 showed a relatively narrow peak with low PET signal intensity, the probability distribution curve in XP945 was wide and right-shifted, suggestive of heterogeneous PD-L1 expression within the tumor (Fig. 3B, Supplementary Table S2).

[^{89}Zr]Zr-DFO-ATZ uptake in tumorgrafts correlates with treatment outcome

Among the TGs included in this study, there were 4 derived from metastatic sites and 3 of these patients received ICI therapy. Among the rest, XP945 was generated from a T4 tumor invading into the adrenal gland that was resected and also received ICI therapy for metastatic disease. In total, four (50%) of TG lines in this study were derived from patients who received ICI therapy. Clinical characteristics of these patients at the time of ICI initiation are summarized in Table 2. One patient received ICI as first line therapy, while the remainder received ICI as 3rd or later line. All patients received nivolumab monotherapy and one had nivolumab/ipilimumab combination after progression on nivolumab monotherapy. Best responses to ICI included a partial response in one patient, a mixed response in one patient, and progressive disease in two patients (Fig. 4A and 4B). The TG derived from patient XP945, who had a partial response to ICI (20), had the highest levels of immunoPET signal among all 4 TGs examined (Fig. 4B) (corresponding to high PD-L1 by IHC on both the TG and patient tissue). Interestingly, patient XP818 experienced a mixed response to immunotherapy with shrinkage of pulmonary lesions but progression in the central nervous system (CNS). The XP818 TG line was derived from a new lesion that developed on therapy (post ICI) and had very low PD-L1 enhancement by immunoPET which corresponded with 0% PD-L1 expression by IHC.

Discussion

ImmunoPET, which evolved from conventional radioimmunodiagnostics, is a promising imaging technique for *in vivo* tumor characterization, with potential applications in ICI treatment selection and monitoring treatment response (13,29,30). IHC-measured PD-L1 expression has been shown to predict ICI response in several tumor types, but there is conflicting evidence for RCC (14,16,31). We hypothesized that this may be due to limitations of tissue-based PD-L1 analyses which oftentimes rely on minute tumor fragments or archival tissue that may not be representative of the current disease in the patient. ImmunoPET, which delivers noninvasive information for all lesions in real-time, offers a potential alternate strategy. In one clinical study evaluating ATZ monotherapy in a variety of tumor types, immunoPET with [^{89}Zr]Zr-DFO-ATZ was found to correlate more strongly with treatment response than PD-L1 expression by IHC (19). However, the utility of immunoPET in RCC remains to be determined. Herein, we report preclinical data evaluating immunoPET with [^{89}Zr]Zr-DFO-ATZ for noninvasive PD-L1 imaging in RCC patient derived TG models expressing a wide range of PD-L1.

While the preparation of [^{89}Zr]Zr-DFO-ATZ has been previously reported by us (20) and others (19,27,32), we observed batch-to-batch variations in the immunoreactivity and radiolabeling efficiency of the antibody conjugates. We found that the main determinant is the molar ratio of DFO:ATZ, which is preferably 1:1. At this ratio, the binding affinity of DFO-ATZ to PD-L1 was indistinguishable to that of intact ATZ as measured by a cell-based assay. The analytical method we developed herein using LC-MS provides a rapid measurement to assess the “apparent number of DFO per ATZ”, which assists in the quality control of DFO-ATZ synthesis and reduces the batch-to-batch variation. This method has been implemented in our ongoing clinical trial (NCT04006522).

Tumorgrafts, which preserve histological and molecular features from the corresponding patient tumors, are an invaluable tool for the development of diagnostic and therapeutic agents (21). Using such TGs, we were able to evaluate immunoPET with [^{89}Zr]Zr-DFO-ATZ in RCC. Kinetic analyses determined that optimal timing for immunoPET imaging was ~ 7 days following tracer administration. Inasmuch as ATZ can bind to mouse PD-L1, this platform also allowed the measurement of [^{89}Zr]Zr-DFO-ATZ uptake across normal tissues. Consistent with this notion, high levels were observed in the spleen. Of note, this is likely driven by the fact that the Fab portion of the mAb is mutated. In contrast, [^{89}Zr]Zr-DFO-ATZ uptake in the muscle was relatively low and remained constant over time. Thus, we normalized tumor uptake to muscle uptake. The T/M ratios strongly correlated with PD-L1 IHC measurements on explanted tissues. Absolute tumor uptake of [^{89}Zr]Zr-DFO-ATZ also showed a significant, albeit weaker, correlation.

We retrospectively assessed the clinical responses of four patients who received ICI therapy. PD-L1 expression in the TGs, both by IHC and immunoPET, tended to correlate with clinical outcomes. One noteworthy exception is the patient from whom XP818 was derived. This patient had a mixed response to therapy with shrinkage in pulmonary metastases but progression in the CNS. The corresponding TG line was derived from a spinal cord metastasis that had developed on therapy and had low PD-L1 levels (by both IHC and radiotracer uptake).

Heterogeneity may exist not only across sites of disease, but also within tumors (33,34). To address whether immunoPET can identify this heterogeneous PD-L1 target expression, we performed voxel-based quantitative analyses. Interestingly, even in the absence of PD-L1 expression, the intratumoral distribution of the radiotracer was wide. Additionally, there was not only a rightward shift, but also a broadening of the radiotracer uptake distribution in PD-L1 expressing tumors, and the difference between the two distribution curves was statistically significant. This suggests that immunoPET may also be helpful in characterizing intratumoral heterogeneity, which was indeed observed in a clinical trial participant recently reported by us (21).

Tumoral PD-L1 expression can be labile and dependent on several variables (35–37). The PD-1/PD-L1 pathway has been reported to have an inverse relationship with the vascular endothelial growth factor (VEGF) pathway in ccRCC (38). Inflammatory cytokines, such as interferon gamma (IFNγ) and tumor necrosis factor alpha (TNFα), upregulate PD-L1 (39). Moreover, PD-L1 expression can be altered by antineoplastic agents (40,41) as well as radiotherapy (42). Inasmuch as immunoPET is noninvasive, it can be used to probe *in vivo* determinants of PD-L1 expression over time. In addition, immunoPET may also shed light into mechanisms of resistance by identifying instances of PD-L1 downregulation, as well as resistant lesions that retain PD-L1 expression (suggesting an alternative mechanism of resistance) (15,43,44).

This study has several limitations. First, although both immunoPET and IHC were intended for the measurement of PD-L1, the imaging and *ex vivo* procedures were neither performed at the same time, nor in the same biological context. As PD-L1 expression is dynamic and heterogeneous in tumors, discrepancies are expected between the two

measurements. This was particularly true in tumors with low PD-L1 expression wherein the immunoPET readouts were higher than the IHC measurements. Possible explanations include radiotracer retention in the tumor blood pool and potential residualization of ^{89}Zr-containing catabolites in tumor cells after lysosomal degradation of [^{89}Zr]Zr-DFO-ATZ (45). Whether these issues will be confounding factors in patients remains to be seen, but they could limit the ability to distinguish small differences in PD-L1 levels. Nevertheless, our double-blinded study revealed a statistically significant ($p = 0.0014$) association between immunoPET quantification of PD-L1 expression and its corresponding IHC. Additionally, the clinically relevant thresholds of immunoPET uptake remain to be determined. PD-L1 is expressed in a variety of cell types, and the contribution of the tumor *vs.* tumor microenvironment compartments to the overall uptake cannot be dissected using [^{89}Zr]Zr-DFO-ATZ immunoPET. To adjust for this, we used the CPS IHC scoring method, which reports PD-L1 expression across all cell types, and not the tumor proportion score (23,46,47). Finally, though patient derived TG mouse models have been shown to recapitulate the host (patient) molecular features, they are grown in immunocompromised mouse hosts, which limits their application in evaluating ICIs (21). Despite these limitations, immunoPET appears to be capable of monitoring PD-L1 expression in RCC and holds promising potential as a predictive biomarker. Further, the studies performed in this work supported an FDA IND application and a clinical trial that is currently accruing patients (NCT04006522).

Supplementary Material

Refer to Web version on PubMed Central for supplementary material.

Acknowledgements

We acknowledge the patients that donated tissues enabling these studies. This research was supported by grants from the V Foundation (T2018–011, I. Bowman, X. Sun, J. Brugarolas), Cancer Prevention and Research Institute of Texas (RP110771 & RP170638, X. Sun), the Kidney Cancer Research Program of the Department of Defense (W81XWH-19–1-0711, X. Sun), and National Institutes of Health (P50CA196516, A, Christie, P. Kapur, J. Brugarolas). We acknowledge the services provided by the Tissue Shared Resource at UT Southwestern, which is supported in part by the Harold C. Simmons Cancer Center through an NCI Cancer Center Support Grant, P30CA142543.

References

1. Siegel RL, Miller KD, Fuchs HE, Jemal A. Cancer statistics, 2022. CA Cancer J Clin 2022;72:7–33 doi 10.3322/caac.21708. [PubMed: 35020204]
2. Motzer RJ, Tannir NM, McDermott DF, Arén Frontera O, Melichar B, Choueiri TK, et al. Nivolumab plus Ipilimumab versus Sunitinib in Advanced Renal-Cell Carcinoma. N Engl J Med 2018;378:1277–90 doi 10.1056/NEJMoa1712126. [PubMed: 29562145]
3. Rini BI, Plimack ER, Stus V, Gafanov R, Hawkins R, Nosov D, et al. Pembrolizumab plus Axitinib versus Sunitinib for Advanced Renal-Cell Carcinoma. N Engl J Med 2019;380:1116–27 doi 10.1056/NEJMoa1816714. [PubMed: 30779529]
4. Motzer RJ, Penkov K, Haanen J, Rini B, Albiges L, Campbell MT, et al. Avelumab plus axitinib versus sunitinib for advanced renal-cell carcinoma. N Engl J Med 2019;380:1103–15. [PubMed: 30779531]
5. Choueiri TK, Powles T, Burotto M, Escudier B, Bourlon MT, Zurawski B, et al. Nivolumab plus Cabozantinib versus Sunitinib for Advanced Renal-Cell Carcinoma. N Engl J Med 2021;384:829–41 doi 10.1056/NEJMoa2026982. [PubMed: 33657295]

6. Motzer R, Alekseev B, Rha SY, Porta C, Eto M, Powles T, et al. Lenvatinib plus Pembrolizumab or Everolimus for Advanced Renal Cell Carcinoma. N Engl J Med 2021;384:1289–300 doi 10.1056/NEJMoa2035716. [PubMed: 33616314]
7. Motzer RJ, Escudier B, McDermott DF, George S, Hammers HJ, Srinivas S, et al. Nivolumab versus Everolimus in Advanced Renal-Cell Carcinoma. N Engl J Med 2015;373:1803–13 doi 10.1056/NEJMoa1510665. [PubMed: 26406148]
8. Topalian Suzanne L, Drake Charles G, Pardoll Drew M. Immune Checkpoint Blockade: A Common Denominator Approach to Cancer Therapy. Cancer Cell 2015;27:450–61 doi 10.1016/j.ccell.2015.03.001. [PubMed: 25858804]
9. Festino L, Botti G, Lorigan PC, Masucci G, Hipp J, Horak C, et al. Cancer Treatment with Anti-PD-1/PD-L1 Agents: Is PD-L1 Expression a Biomarker for Patient Selection? Drugs 2016;76:925–45 doi 10.1007/s40265-016-0588-x. [PubMed: 27229745]
10. Pardoll DM. The blockade of immune checkpoints in cancer immunotherapy. Nat Rev Cancer 2012;12:252–64. [PubMed: 22437870]
11. Chinai JM, Janakiram M, Chen F, Chen W, Kaplan M, Zang X. New immunotherapies targeting the PD-1 pathway. Trends Pharmacol Sci 2015;36:587–95 doi 10.1016/j.tips.2015.06.005. [PubMed: 26162965]
12. Wang X, Teng F, Kong L, Yu J. PD-L1 expression in human cancers and its association with clinical outcomes. Onco Targets Ther 2016;9:5023–39 doi 10.2147/OTT.S105862. [PubMed: 27574444]
13. Twomey JD, Zhang B. Cancer Immunotherapy Update: FDA-Approved Checkpoint Inhibitors and Companion Diagnostics. AAPS J 2021;23:39 doi 10.1208/s12248-021-00574-0. [PubMed: 33677681]
14. Santoni M, Massari F, Di Nunno V, Conti A, Cimadamore A, Scarpelli M, et al. Immunotherapy in renal cell carcinoma: latest evidence and clinical implications. Drugs Context 2018;7:212528–28 doi 10.7573/dic.212528. [PubMed: 29899754]
15. Moreira M, Pobel C, Epaillard N, Simonaggio A, Oudard S, Vano Y-A. Resistance to cancer immunotherapy in metastatic renal cell carcinoma. Cancer Drug Resistance 2020;3:454–71 doi 10.20517/cdr.2020.16. [PubMed: 35582435]
16. Xu W, Atkins MB, McDermott DF. Checkpoint inhibitor immunotherapy in kidney cancer. Nat Rev Urol 2020;17:137–50 doi 10.1038/s41585-020-0282-3. [PubMed: 32020040]
17. Torlakovic E, Lim HJ, Adam J, Barnes P, Bigras G, Chan AWH, et al. "Interchangeability" of PD-L1 immunohistochemistry assays: a meta-analysis of diagnostic accuracy. Modern Pathology 2020;33:4–17 doi 10.1038/s41379-019-0327-4. [PubMed: 31383961]
18. Sholl LM, Aisner DL, Allen TC, Beasley MB, Borczuk AC, Cagle PT, et al. Programmed Death Ligand-1 Immunohistochemistry-A New Challenge for Pathologists: A Perspective From Members of the Pulmonary Pathology Society. Archives of Pathology and Laboratory Medicine 2016;140:341–44. [PubMed: 26780537]
19. Bensch F, van der Veen EL, Lub-de Hooge MN, Jorritsma-Smit A, Boellaard R, Kok IC, et al. ^{89}Zr-atezolizumab imaging as a non-invasive approach to assess clinical response to PD-L1 blockade in cancer. Nat Med 2018;24:1852–58 doi 10.1038/s41591-018-0255-8. [PubMed: 30478423]
20. Vento J, Mulgaonkar A, Woolford L, Nham K, Christie A, Bagrodia A, et al. PD-L1 detection using ^{89}Zr-atezolizumab immuno-PET in renal cell carcinoma tumorgrafts from a patient with favorable nivolumab response. J Immunother Cancer 2019;7:144 doi 10.1186/s40425-019-0607-z. [PubMed: 31155004]
21. Elias R, Tcheuyap VT, Kaushik AK, Singla N, Gao M, Reig Torras O, et al. A renal cell carcinoma tumorgraft platform to advance precision medicine. Cell Rep 2021;37:110055 doi 10.1016/j.celrep.2021.110055. [PubMed: 34818533]
22. Syed AK, Woodall R, Whisenant JG, Yankeelov TE, Sorace AG. Characterizing Trastuzumab-Induced Alterations in Intratumoral Heterogeneity with Quantitative Imaging and Immunohistochemistry in HER2+ Breast Cancer. Neoplasia 2019;21:17–29 doi 10.1016/j.neo.2018.10.008. [PubMed: 30472501]

23. Kulangara K, Zhang N, Corigliano E, Guerrero L, Waldroup S, Jaiswal D, et al. Clinical Utility of the Combined Positive Score for Programmed Death Ligand-1 Expression and the Approval of Pembrolizumab for Treatment of Gastric Cancer. Archives of Pathology & Laboratory Medicine 2018;143:330–37 doi 10.5858/arpa.2018-0043-OA. [PubMed: 30028179]
24. Lam M, Webb KA, O'Donnell DE. Correlation between two variables in repeated measures 1999; Alexandria, VA. American Statistical Association. p 213–18.
25. Chatterjee S, Lesniak WG, Gabrielson M, Lisok A, Wharram B, Sysa-Shah P, et al. A humanized antibody for imaging immune checkpoint ligand PD-L1 expression in tumors. Oncotarget 2016.
26. Jagoda EM, Vasalatiy O, Basuli F, Opina ACL, Williams MR, Wong K, et al. Immuno-PET Imaging of the Programmed Cell Death-1 Ligand (PD-L1) Using a Zirconium-89 Labeled Therapeutic Antibody, Avelumab. Mol Imaging 2019;18:1536012119829986 doi 10.1177/1536012119829986.
27. Moroz A, Lee C-Y, Wang Y-H, Hsiao JC, Sevillano N, Truillet C, et al. A Preclinical Assessment of ^{89}Zr-atezolizumab Identifies a Requirement for Carrier Added Formulations Not Observed with ^{89}Zr-C4. Bioconjug Chem 2018;29:3476–82 doi 10.1021/acs.bioconjchem.8b00632. [PubMed: 30227708]
28. Sivanand S, Peña-Llopis S, Zhao H, Kucejova B, Spence P, Pavia-Jimenez A, et al. A validated tumorgraft model reveals activity of dovitinib against renal cell carcinoma. Sci Transl Med 2012;4:137ra75 doi 10.1126/scitranslmed.3003643.
29. Mestel R Cancer: Imaging with antibodies. Nature 2017;543:743–46 doi 10.1038/543743a. [PubMed: 28358075]
30. Verhaar-Langereis MJ, Zonnenberg BA, de Klerk JMH, Blijham GH. Radioimmunodiagnosis and therapy. Cancer Treat Rev 2000;26:3–10 doi 10.1053/ctrv.1999.0146. [PubMed: 10660488]
31. Davis AA, Patel VG. The role of PD-L1 expression as a predictive biomarker: an analysis of all US Food and Drug Administration (FDA) approvals of immune checkpoint inhibitors. J Immunother Cancer 2019;7:278 doi 10.1186/s40425-019-0768-9. [PubMed: 31655605]
32. Ehlerding EB, Lee HJ, Barnhart TE, Jiang D, Kang L, McNeel DG, et al. Noninvasive Imaging and Quantification of Radiotherapy-Induced PD-L1 Upregulation with 89Zr–Df–Atezolizumab. Bioconjug Chem 2019;30:1434–41. [PubMed: 30973703]
33. Zhong W, Li Y, Yuan Y, Zhong H, Huang C, Huang J, et al. Characterization of Molecular Heterogeneity Associated With Tumor Microenvironment in Clear Cell Renal Cell Carcinoma to Aid Immunotherapy. Front Cell Dev Biol 2021;9 doi 10.3389/fcell.2021.736540.
34. Turajlic S, Xu H, Litchfield K, Rowan A, Chambers T, Lopez JI, et al. Tracking Cancer Evolution Reveals Constrained Routes to Metastases: TRACERx Renal. Cell 2018;173:581–94.e12 doi 10.1016/j.cell.2018.03.057. [PubMed: 29656895]
35. Patel SP, Kurzrock R. PD-L1 Expression as a Predictive Biomarker in Cancer Immunotherapy. Mol Cancer Ther 2015;14:847 doi 10.1158/1535-7163.MCT-14-0983. [PubMed: 25695955]
36. Tang H, Liang Y, Anders RA, Taube JM, Qiu X, Mulgaonkar A, et al. PD-L1 on host cells is essential for PD-L1 blockade–mediated tumor regression. J Clin Investig 2018;128:580–88 doi 10.1172/JCI96061. [PubMed: 29337303]
37. Wei Y, Zhao Q, Gao Z, Lao X-M, Lin W-M, Chen D-P, et al. The local immune landscape determines tumor PD-L1 heterogeneity and sensitivity to therapy. J Clin Investig 2019;129:3347–60 doi 10.1172/JCI127726. [PubMed: 31112529]
38. Joseph RW, Parasramka M, Eckel-Passow JE, Serie D, Wu K, Jiang L, et al. Inverse association between programmed death ligand 1 and genes in the VEGF pathway in primary clear cell renal cell carcinoma. Cancer Immunol Res 2013;1:378–85 doi 10.1158/2326-6066.CIR-13-0042. [PubMed: 24778130]
39. Kondo A, Yamashita T, Tamura H, Zhao W, Tsuji T, Shimizu M, et al. Interferon-gamma and tumor necrosis factor-alpha induce an immunoinhibitory molecule, B7-H1, via nuclear factor-kappaB activation in blasts in myelodysplastic syndromes. Blood 2010;116:1124–31 doi 10.1182/blood-2009-12-255125. [PubMed: 20472834]
40. Ghebeh H, Lehe C, Barhoush E, Al-Romaih K, Tulbah A, Al-Alwan M, et al. Doxorubicin downregulates cell surface B7-H1 expression and upregulates its nuclear expression in breast

cancer cells: role of B7-H1 as an anti-apoptotic molecule. Breast Cancer Res 2010;12:R48 doi 10.1186/bcr2605. [PubMed: 20626886]

41. Zhang P, Su DM, Liang M, Fu J. Chemopreventive agents induce programmed death-1-ligand 1 (PD-L1) surface expression in breast cancer cells and promote PD-L1-mediated T cell apoptosis. Mol Immunol 2008;45:1470–6 doi 10.1016/j.molimm.2007.08.013. [PubMed: 17920123]
42. Deng L, Liang H, Burnette B, Beckett M, Darga T, Weichselbaum RR, et al. Irradiation and anti-PD-L1 treatment synergistically promote antitumor immunity in mice. J Clin Invest 2014;124:687–95 doi 10.1172/JCI67313. [PubMed: 24382348]
43. Nowicki TS, Hu-Lieskovan S, Ribas A. Mechanisms of Resistance to PD-1 and PD-L1 Blockade. Cancer J 2018;24:47–53 doi 10.1097/PPO.0000000000000303. [PubMed: 29360728]
44. Strickler JH, Hanks BA, Khasraw M. Tumor Mutational Burden as a Predictor of Immunotherapy Response: Is More Always Better? Clin Cancer Res 2021;27:1236 doi 10.1158/1078-0432.CCR-20-3054. [PubMed: 33199494]
45. Cheal SM, Punzalan B, Doran MG, Evans MJ, Osborne JR, Lewis JS, et al. Pairwise comparison of ^{89}Zr- and ^{124}I-labeled cG250 based on positron emission tomography imaging and nonlinear immunokinetic modeling: in vivo carbonic anhydrase IX receptor binding and internalization in mouse xenografts of clear-cell renal cell carcinoma. European Journal of Nuclear Medicine and Molecular Imaging 2014;41:985–94 doi 10.1007/s00259-013-2679-1. [PubMed: 24604591]
46. Guo H, Ding Q, Gong Y, Gilcrease MZ, Zhao M, Zhao J, et al. Comparison of three scoring methods using the FDA-approved 22C3 immunohistochemistry assay to evaluate PD-L1 expression in breast cancer and their association with clinicopathologic factors. Breast Cancer Res 2020;22:69 doi 10.1186/s13058-020-01303-9. [PubMed: 32576238]
47. Doroshow DB, Bhalla S, Beasley MB, Sholl LM, Kerr KM, Gnjatic S, et al. PD-L1 as a biomarker of response to immune-checkpoint inhibitors. Nat Rev Clin Oncol 2021;18:345–62 doi 10.1038/s41571-021-00473-5. [PubMed: 33580222]

Translational Relevance

Immune checkpoint inhibitors (ICIs) have revolutionized renal cell carcinoma (RCC) therapy. However, only a subset of patients respond to ICIs and predictive biomarkers are lacking. Unlike other tumor types, tissue-based PD-L1 analyses have not been predictive of ICI response in RCC. We hypothesized that more comprehensive analyses enabled by immuno-positron emission tomography (immunoPET) may overcome the limitations of tissue-based studies. ImmunoPET using ^{89}Zr-labeled atezolizumab allowed noninvasive real-time measurement of PD-L1 in an RCC patient-derived tumorgraft (TG) platform, which supported an investigational new drug (IND) application to the United States Food and Drug Administration (FDA) for an ongoing clinical trial (NCT04006522).

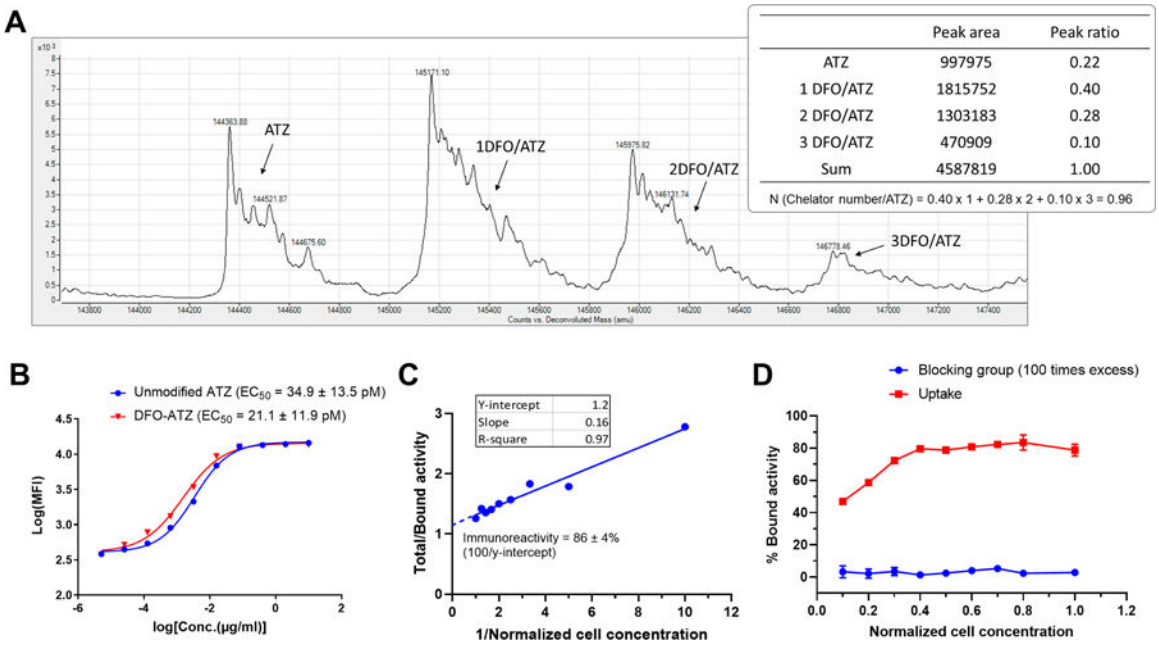

Figure 1. [^{89}Zr]Zr-DFO-ATZ retains PD-L1 binding affinity and specificity.

Panel A: DFO-ATZ conjugate. Representative deconvolution results from LC-MS analysis (n = 3). Plot represents counts (y-axis) *vs.* de-convoluted mass (x-axis). N is the chelator number per ATZ; R_0, R_1, R_2 or R_n is the percentage of the peak area corresponding to DFO-ATZ conjugates with 0, 1, 2, or n DFO chelators, respectively. **Panel B:** Flow cytometry cell binding assay in A20 cells expressing PD-L1. Data are presented as mean ± standard deviation (s.d.); one representative experiment shown (n = 3 in triplicates); MFI: Mean fluorescence intensity; EC_{50} values presented as mean ± standard error of means. **Panel C:** Immunoreactivity assay of [^{89}Zr]Zr-DFO-ATZ in MDA-MB-231 cells expressing PD-L1. Data are presented as mean ± s.d.; one representative experiment shown (n = 6 in triplicates). **Panel D:** Blocking cell assay to test binding specificity of [^{89}Zr]Zr-DFO-ATZ. One hundred times excess unlabeled ATZ (~ 6 ng) was added to the cell suspension along with the [^{89}Zr]Zr-DFO-ATZ (n = 3). Data are presented as mean ± s.d.

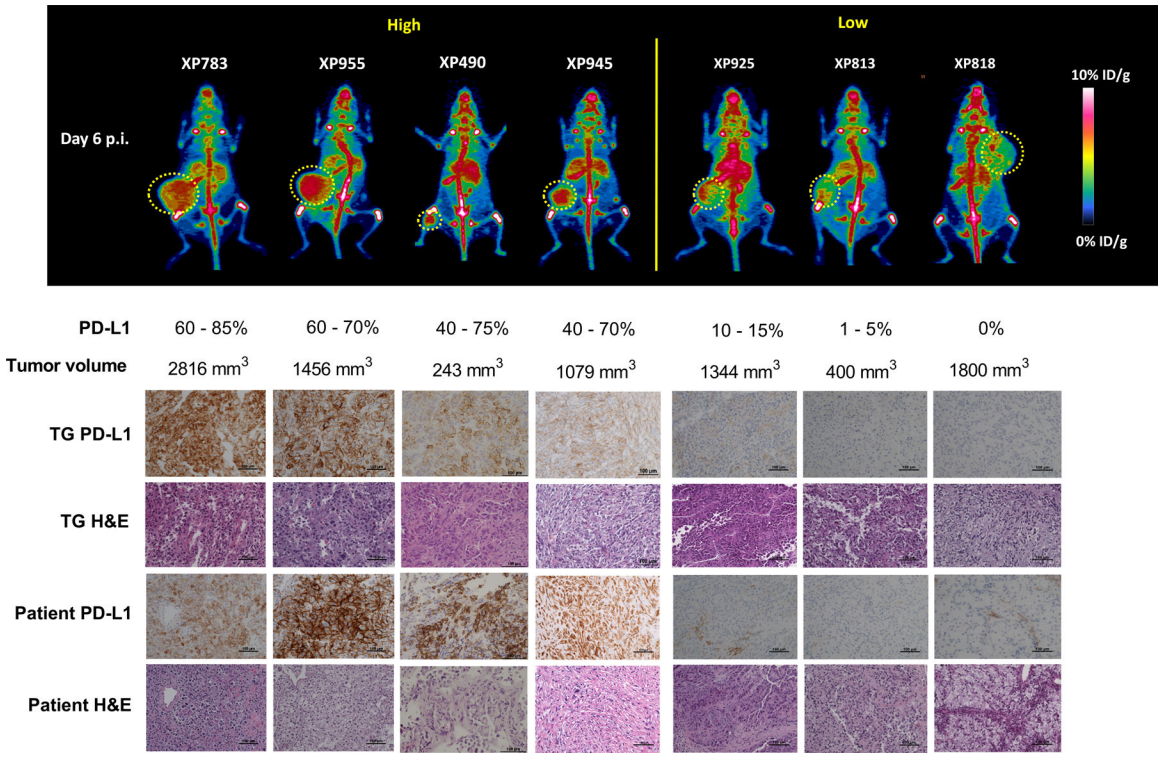

Figure 2. Integrated immunoPET, IHC, and H&E images of tumorgraft (TG) lines and the corresponding patient tumors.

Top panel: Representative whole body maximal intensity projection immunoPET images (posterior view) of mice, one from each group of mice bearing one of the 7 RCC TG lines. Shown below are the corresponding PD-L1 expression range measured by IHC and the volume of the tumor in the mouse (n = 3 – 4 for each line; a single remaining XP258 mouse not included). Tumors are indicated with a yellow lasso. Bottom panel: PD-L1 IHC and hematoxylin and eosin (H&E) staining of the corresponding tumor tissues explanted from the TG models. Patient tumor samples shown as a reference.

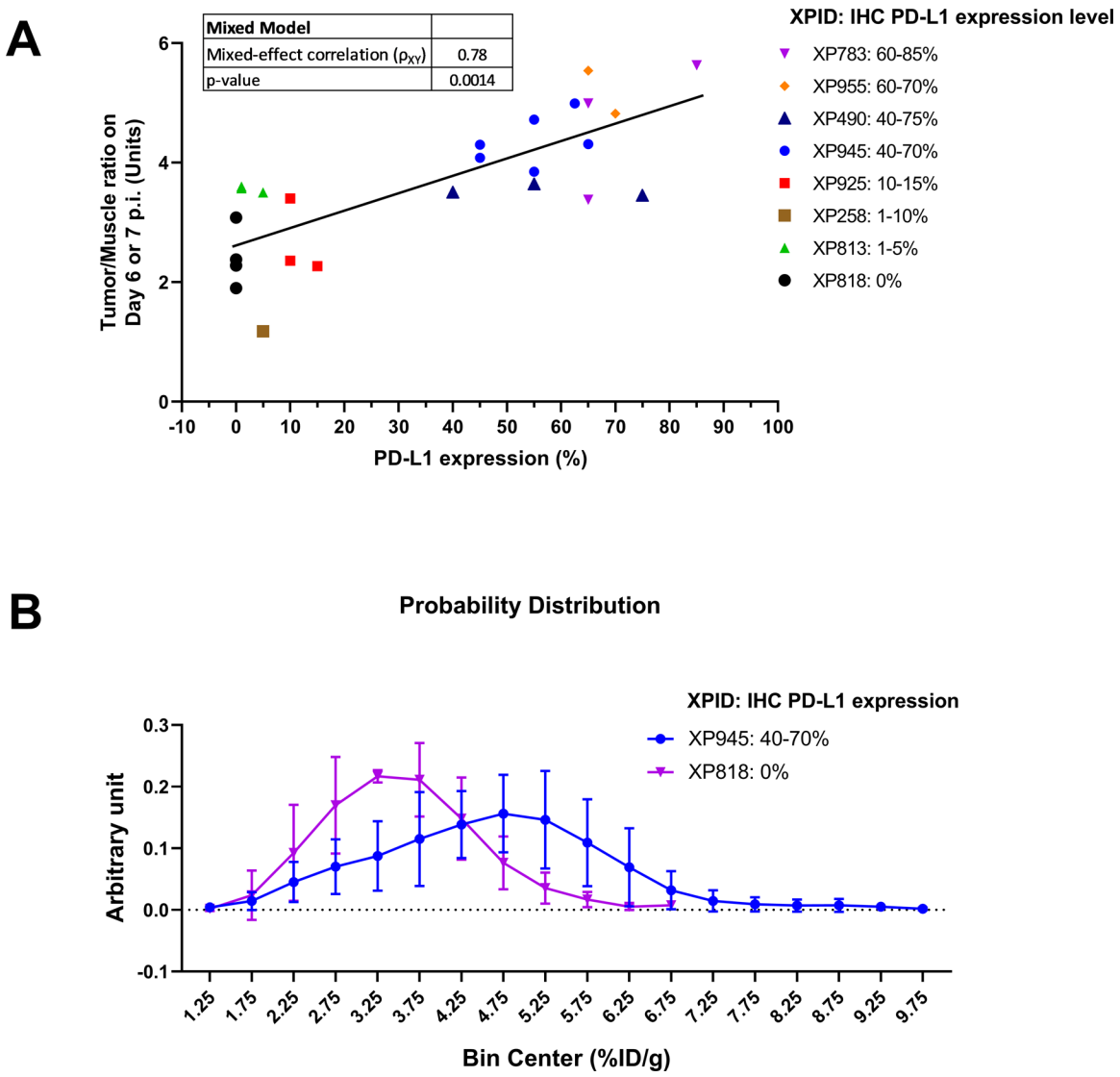

Figure 3. Quantitative immunoPET imaging data analysis.

Panel A: Mixed model statistical analysis of the association between tumor/muscle ratios by immunoPET and PD-L1 expression levels in the corresponding tumors by *ex vivo* IHC. The model accounts for variations among individual mice within a TG line. The data are from 8 RCC TG lines (25 mice were analyzed using SAS 9.4 with an alpha value of 0.05); ρ_{XY} = mixed model correlation. **Panel B:** Comparative probability distribution analysis of heterogeneous PD-L1 expression in two TG lines: XP945 (40 – 70% PD-L1 IHC, n = 6) *vs.* XP818 (0% PD-L1 IHC, n = 4). The bin frequency of the distribution histogram was normalized to the total number of immunoPET voxels analyzed. A mixed model analysis was performed to compare the overall difference in tumor uptake voxel distribution between the two TG lines (p = 0.0024). Muscle uptake was included in the model as background signal (non-specific uptake) in each mouse. All data are presented as mean ± s.d.

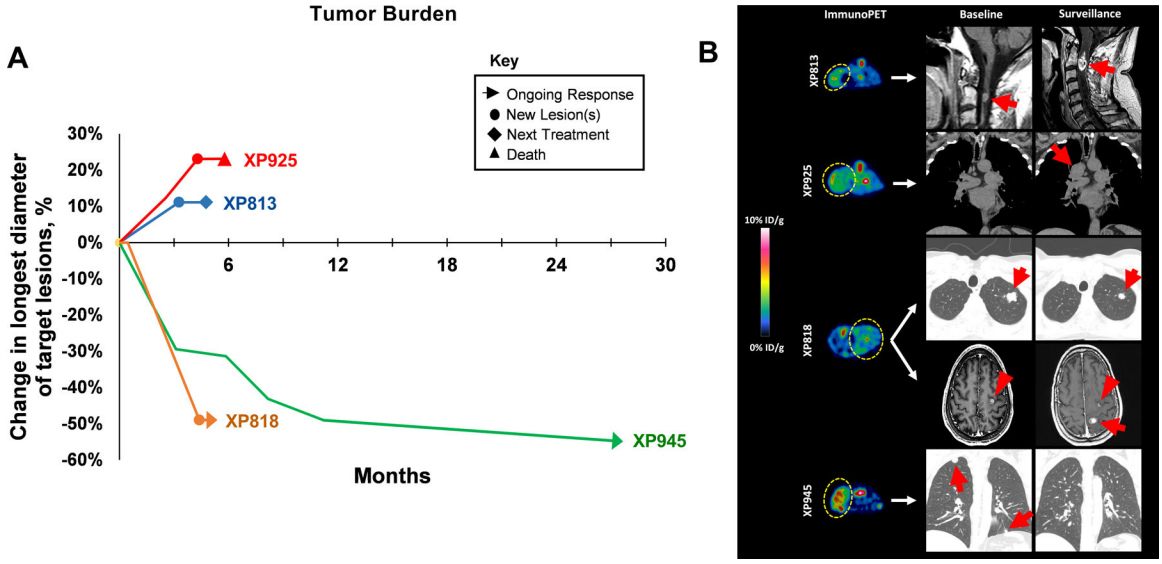

Figure 4. Clinical outcomes to ICI therapy and correlation to PD-L1 expression by immunoPET.

Panel A: Illustration of tumor burden over time after ICI initiation. Tumor burden was determined as the sum of target lesions using RECIST v1.1 principles. **Panel B:** Representative immunoPET images of TG lines and clinical images from corresponding patients at baseline and on follow-up after ICI. Yellow lassos indicate tumors on PET images and red arrows/arrowheads point to CT/MRI-identified lesions. Patients corresponding to XP813 and XP925 demonstrated progressive disease as best response. Progressive spinal cord lesion shown was subsequently resected and became source of TG line. Patient XP818 had a mixed response, with shrinkage of lung nodules but progression with new brain metastases. Patient XP945 had a lasting partial response (20).

Table 1.

Baseline clinicopathologic characteristics at the time of tumorgraft generation

XPID	XP258	XP490	XP783	XP813	XP818	XP925	XP945	XP955
Sex	F	M	M	M	M	M	M	F
Race	Black	White	White	White	White	White	White	White
Ethnicity	Non-Hispanic	Non-Hispanic	Hispanic	Non-Hispanic	Non-Hispanic	Non-Hispanic	Non-Hispanic	Hispanic
Age (years)	50	64	56	57	52	58	49	63
Tumor Source	Primary	Primary	Metastasis	Metastasis	Metastasis	Metastasis	Primary	Primary
Tumor Site	Kidney	Kidney	Bone	Spinal Cord	Spinal Cord	RP mass	Adrenal[a]	Tumor Thrombus
Histology	ccRCC	ccRCC	ccRCC	ccRCC	ccRCC	pRCC	ccRCC	ccRCC
pT stage	3a	3a	N/A	N/A	N/A	N/A	4	3a
Grade	4	4	4	3	3	3	4	4
Sarcomatoid Features	Yes	Yes	Yes	No	No	No	Yes	No
Rhabdoid Features	No	Yes	No	No	No	No	No	No
Prior Treatment	None	None	Pazo	Pazo, Eve, Axi, Bev, Nivo	HDIL2, Axi, Nivo, Nivo+Ipi	None	None	None
PD-L1 IHC % (Patient Tumor)	0	25	50	0	1	15	30	75–80
PD-L1 IHC % (TG) [b]	1–10	40–75	60–85	1–5	0	10–15	40–70	60–70

a: via direct invasion of primary tumor

b: range represents variation in PD-L1 expression across mice within the same XP line (i.e., derived from the same parent tumor).

Abbreviations: Axi, axitinib; Bev, bevacizumab; Eve, everolimus; F, female; HDIL2, high dose Interleukin 2; Ipi, ipilimumab; M, male; N/A, Not Applicable; Nivo, nivolumab; pRCC, papillary renal cell carcinoma; Pazo, pazopanib; pT, pathologic T stage; RP, retroperitoneal; XPID, xenograft project ID.

Table 2.

Clinical characteristics at the time of ICI initiation

XPID	Source	Histologic Subtype	IMDC score	Prior Therapy	ICI	Best OR	Patient Tumor PD-L1 IHC (%)	TG PD-L1 IHC (%)	PFS (mos.)
XP813	Met. (Spinal Cord)	ccRCC	Poor	Pazo, Eve, Axi, Bev	Nivo	PD	0[a]	1 – 5	3.3
XP925	Met. (RP Mass)	pRCC	Fav.	None	Nivo	PD	15	10 – 15	4.30
XP818	Met. (Spinal Cord)	ccRCC	Poor	HDIL2, Axi	Nivo, Nivo+Ipi	MR	1[a]	0	5.38
XP945	Primary	ccRCC	Int.	HDIL2, Pazo	Nivo	PR	30	40 – 70	27.7

a: tumorgraft lines generated from progressive lesions after ICI.

Abbreviations: PFS (mos), progression free survival in months from the time of starting ICI therapy; Axi, axitinib; Bev, bevacizumab; Eve, everolimus; Fav., favorable; HDIL2, High-Dose Interleukin 2; Int, intermediate; mos., months; MR, mixed response; Pazo, Pazopanib; PD, progressive disease; PFS, progression free survival; PR, partial response; RP, retroperitoneal; XPID, xenograft project line ID; Met., metastases; OR, Objective response.